Coherent radar imaging of mesosphere summer echoes: Influence of radar beam pattern and tilted structures on atmospheric echo center

Jenn-Shyong Chen,[1] Peter Hoffmann,[2] Marius Zecha,[2] and Cheng-Hsiung Hsieh[3]

[1] Multiple echo centers of a mesosphere-summer-echo layer (MSE) observed by the six-receiver OSWIN VHF radar (54.1°N, 11.8°E) were examined with the coherent radar imaging (CRI) technique. The data were collected by different observational modes: vertical and oblique radar beams with the receiving configurations of 3×2, 6×1 (meridional alignment) and 1×6 (zonal alignment) antenna groups. The unique receiving configurations of meridional and zonal aligned antenna groups reveal that the echo centers clustered in three distinct groups above the range height of ~86 km. The central group of echo centers was around the direction of radar beam; however, the off-zenith angles of the two side groups, ranging between several and 20 degrees, increased with ascendant range height. Two potential causes of the echoes in the two side groups were examined on the basis of simulation calculation, namely, tilted structures in the layer and additionally, the influence of radar beam pattern. It is indicated that some echoes, originating from the lower part (<~86 km) of the layer, can enter from the first and second sidelobes of the radar beam pattern and then be received at higher range gates (>~86 km) at larger off-zenith angles. The tilted structures, which are considered to be related to wave activities, can also produce the features similar to the observations. This is demonstrated by simulation calculation with wavy reflecting layers, in which the waves are supposed to modulate the multiple reflecting layers, with increasing amplitudes, tilted shapes, asynchronous phases, and horizontal travel.

1. Introduction

[2] Strong VHF/UHF radar echoes have been commonly observed in the vicinity of the mesopause height (~86 km) during summertime. These echoes are referred to as polar mesosphere summer echoes (PMSE) and mesosphere summer echoes (MSE) in the literature, depending on their emersion places being in the polar or at midlatitude, respectively [e.g., *Czechowsky et al.*, 1979; *Ecklund and Balsley*, 1981; *Röttger et al.*, 1988; *Reid et al.*, 1989; *Czechowsky and Rüster*, 1997; *Huaman and Balsley*, 1998; *Hoffmann et al.*, 1999; *Latteck et al.*, 1999; *Zecha et al.*, 2003; *Bremer et al.*, 2003]. The PMSE and MSE were first detected in the northern hemisphere. Recently they have also been observed in the southern hemisphere [*Woodman et al.*, 1999; *Morris et al.*, 2004, 2006].

[3] PMSE and MSE have drawn much attention from scientists due to their unusual features as well as their close relationships with global circulation of the atmosphere, variations of temperature and water vapor in the mesosphere, and so on. In view of this, long-term observation of the PMSE/MSE can be useful as an indicator of global change. The formation of PMSE/MSE is related to the charged particles and extremely low temperature. Reviews about experimental and model results concerning PMSE/MSE can be found in the works of *Cho and Kelley* [1993], *Cho and Röttger* [1997], and *Rapp and Lübken* [2004].

[1]Department of Computer and Communication Engineering, Chienkuo Technology University, Taiwan.
[2]Leibniz-Institut für Atmosphärenphysik, Kühlungsborn, Germany.
[3]Department of Computer Science and Information Engineering, Chaoyang University of Technology, Taiwan.

[4] Recently, the multiple-receiver radar interferometry, termed coherent radar imaging (CRI) in the MST radar community [*Woodman*, 1997], has been applied to the PMSE/MSE, providing extra inspection of aspect sensitivity and wave activities from the view of multiple scattering/reflecting centers of the echoes [*Yu et al.*, 2001; *Chilson et al.*, 2002; *Chen et al.*, 2004]. To go further, this study extended the investigation made by *Chen et al.* [2004], with the MSE data observed by the OSWIN 53.5 MHz radar. The MSE data were collected by different observational modes: vertical and oblique radar beams with the receiving configurations of 3×2, 6×1 (meridional alignment) and 1×6 (zonal alignment) antenna groups (see section 2 for the details). Part of the data was examined by *Chen et al.* [2004]; however, this study examined the other data observed alternately in the same period and oriented towards different concerns. In the observations with the meridional and zonal aligned antenna groups, many echoes were found to be at large off-zenith angles (ranging between several and 20 degrees) and their off-zenith angles became larger as range height increased. Such large incident angles of echoes were not reported in the PMSE/MSE studies with the CRI before. Therefore, it is worthy of studying these echoes to inspect their potential causes of generation and improve our understanding of using CRI technique with different transmitting/receiving modes. We will consider two aspects: radar beam pattern and tilted structures in the MSE layer.

[5] Previous works of CRI [e.g., *Yu et al.*, 2001; *Chilson et al.*, 2002] concentrated on small zenith angles of echoing locations within the beam width. For large zenith angles outside the main beam, however, the error of the estimated echoing locations may be significant due to the transmitting-receiving beam pattern, which should be examined in more detail. As for the tilted structures, they can be partly related to wave activities. In the literature, steep wave structures were detected in the PMSE with a very narrow radar beam ($\sim 1°$), which were verified mainly by significant discontinuous offsets or jumps in the Doppler frequency [*Röttger et al.*, 1988, 1990]. In addition, off vertical and multiple reflecting angles owing to gravity waves with different wavelengths and amplitudes were demonstrated by either simulation or observation [*Röttger et al.*, 1990; *Meek and Manson*, 1992; *Yu et al.*, 2001]. Referring to these studies, we made an extended simulation of wave-induced reflection points by considering growing wave amplitudes [*Mobbs*, 1985; *Weinstock*, 1986]. We intend to describe another possibility of the echoes at large off-zenith angles.

[6] To carry out the above studies, it is needed to estimate the angular locations of the echoes from the brightness distribution of CRI. However, we found that multiple brightness centers occur very frequently in our data and their angular locations are difficult to determine

by fitting with a two-dimensional Gaussian function. In view of this, a contour-based approach was developed in this study to locate multiple brightness centers. This locating approach is very helpful for our present CRI study.

[7] This paper is organized as follows: in section 2 we describe the OSWIN VHF radar, the experimental data, the Capon method which we use to process the multiple-receiver radar data, and the locating approach to estimate brightness centers; in section 3 the CRI brightness distribution and the locating results are presented; in section 4 we examine the effect of radar beam pattern on the estimated echo centers, as well as possible origination of the echo centers observed at large off-zenith angles; our conclusions are stated in section 5, where we also propose some ideas for future tasks, especially to quantize the influence of the discussed causes at large-off zenith angles.

2. Instruments and Analysis Methods

2.1. Instruments

[8] The OSWIN VHF radar (54.1°N, 11.8°E; Germany) is operated at a central frequency of 53.5 MHz. The whole 12×12 Yagi antenna array can be partitioned into six receiving antenna groups where each group consists of 4×6 or 2×12 or 12×2 Yagis, as indicated in Figure 1a. These three different arrangements are termed SA, COL, and ROW modes, respectively. The whole antenna array is used for transmission, resulting in a transmitted half-power beam width of $6°$ in zonal and meridional directions both. However, the half-power beam widths in zonal and meridional directions for each receiving antenna group of the SA, COL, and ROW modes are about, respectively, $12°$ and $14.6°$, $6°$ and $42.8°$, and $42.8°$ and $6°$. Combined attenuations of vertical/$7°$-oblique transmitting and ROW-mode receiving patterns are displayed in Figures 1b and 1c, which will be discussed in more detail in the section 4.1. For more descriptions of this radar, see the website http://www.iap-kborn.de or *Latteck et al.* [1999].

[9] The data examined in this study were collected with the SA, COL and ROW modes alternately, in which the sequence of operation modes was the SA (vertical), the COL (vertical, $7°$-north, $7°$-south), and the ROW (vertical, $7°$-east, $7°$-west) modes. The time duration of one operating cycle was about 2 minutes. Sampling time was ~ 0.0151 s, and 1024 samples were collected for each mode and beam direction during one operating cycle. Both sampling resolution and sampling step in range were 300 m.

2.2. Capon Method

[10] To deal with the multiple-receiver echoes, we employed Capon's method. Although other processes

(a)
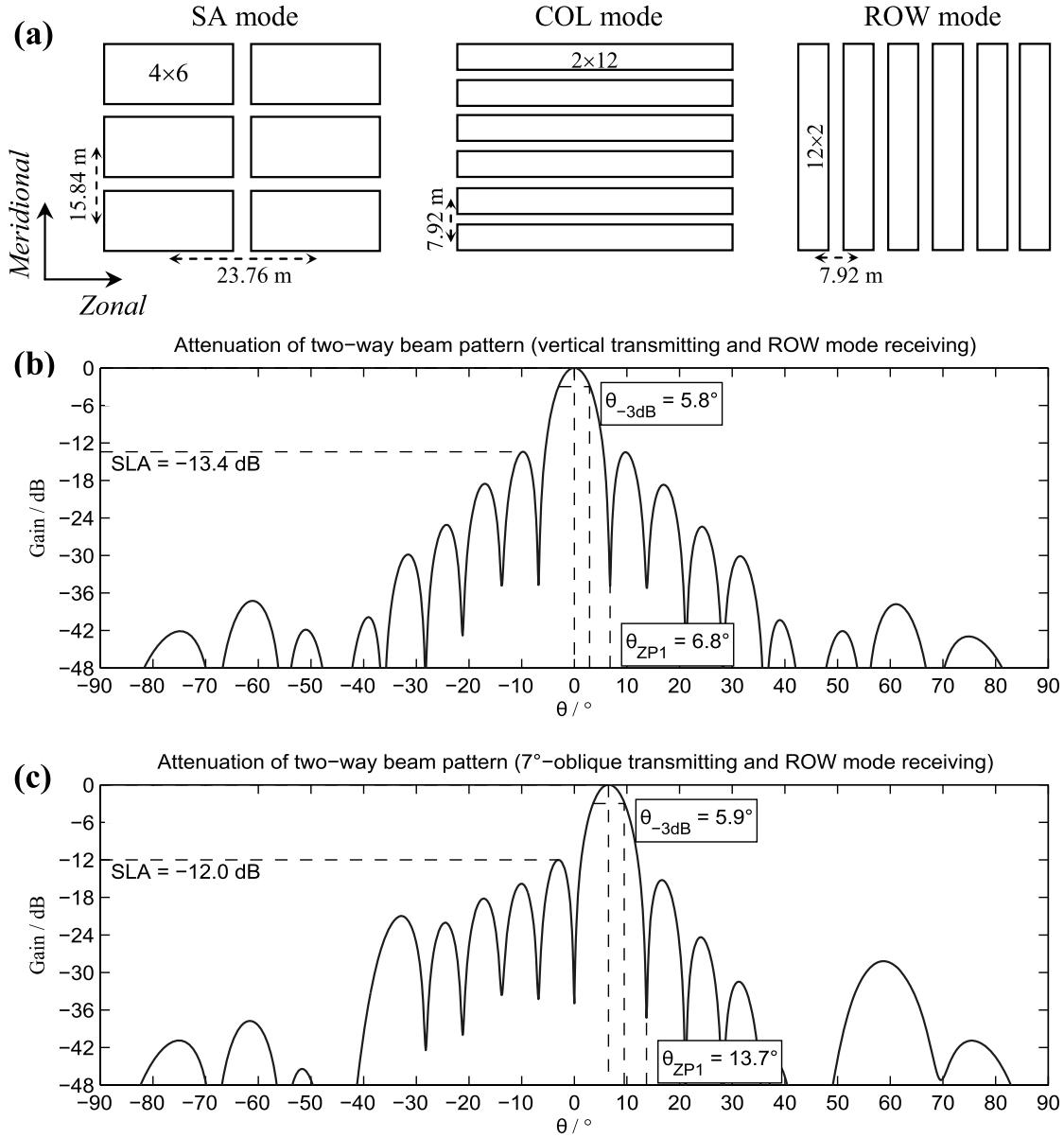
Figure 1. (a) Six partitions of OSWIN VHF radar array for receiving, where the spacing between adjacent receiving antenna groups of COL or ROW mode is 7.92 m, and the spacings between adjacent receiving antenna groups in zonal and meridional direction of SA mode are, respectively, 23.76 m and 15.84 m. (b) Two-way beam pattern with vertically transmitted radar beam and ROW-mode reception. (c) Two-way beam pattern with 7°E-oblique transmitted radar beam and ROW-mode reception.

such as the Fourier method [*Kudeki and Sürücü*, 1991; *Huang et al.*, 1995], the maximum entropy method [*Hysell*, 1996; *Hysell and Woodman*, 1997], and the multiple-signal classification (MUSIC) algorithm [*Hélal et al.*, 2001] are also available, Capon's method has been demonstrated to execute easily and still results in good products in CRI [*Yu et al.*, 2000]. Capon's method estimates the average signal power density (termed brightness distribution) as a function of angle (and Doppler shift if needed); readers can see *Capon* [1969]

and *Palmer et al.* [1998] for the details of this method. In this study the equations without Doppler sorting for estimating the brightness distribution are

$$B(\boldsymbol{k}) = \frac{1}{\mathbf{e}^H \mathbf{R}^{-1} \mathbf{e}}, \tag{1a}$$

$$\mathbf{R} = \begin{bmatrix} R_{11} & R_{12} & \dots & R_{1n} \\ R_{21} & R_{22} & \dots & R_{2n} \\ . & . & . & . \\ R_{n1} & R_{n2} & \dots & R_{nn} \end{bmatrix}, \tag{1b}$$

$$\mathbf{e} = \begin{bmatrix} \mathrm{e}^{\mathrm{j}\boldsymbol{k}\cdot\boldsymbol{D}_1} & \mathrm{e}^{\mathrm{j}\boldsymbol{k}\cdot\boldsymbol{D}_2} \dots \mathrm{e}^{\mathrm{j}\boldsymbol{k}\cdot\boldsymbol{D}_\mathrm{n}} \end{bmatrix}^T, \tag{1c}$$

where B is the brightness distribution, $\boldsymbol{k}$ is the wavenumber vector in the direction where the brightness is to be estimated, $\boldsymbol{k} = (2\pi/\lambda)[\sin\theta\sin\varphi, \sin\theta\cos\varphi, \cos\theta]$, λ is the radar wavelength, θ and φ are, respectively, the zenithal and azimuthal angles. The superscript H in (1a) represents Hermitian operator. $\boldsymbol{D}_\mathrm{n}$ is the central position vector of the nth receiving antenna group. R_{ij} is the zero-lag cross-correlation function of the signals received by receivers i and j. Once the brightness distribution, $B(\boldsymbol{k})$, is obtained, the respective positions of the brightness centers will be estimated for further studies, as described in the next subsection.

2.3. Locating Approach to Angular Positions of Brightness Centers

[11] For the situation of a single-maximum brightness distribution, we usually use a two-dimensional Gaussian fitting for the SA mode and one-dimensional Gaussian fitting for the COL and ROW modes to estimate the position of the brightness maximum (echo center). For multiple brightness maxima, however, the Gaussian fitting cannot work well. In view of this, we employed a contour-based approach to locate the multiple maxima in the brightness distribution, which enable us to deal with a lot of CRI data and perform statistical examination.

[12] Many computing packages that provide contour functions can achieve the purpose, for example, the built-in function $[\mathbf{C}, h] = \mathrm{contour}(\mathbf{B}, n)$ in the MATLAB software, where $\mathbf{B}$ is the two-dimensional brightness distribution, n is the number of contour levels and $\mathbf{C}$ is a matrix containing the coordinates of all contour lines. When the first and the last coordinates of a contour line are the same, the contour line must be a closed curve. After obtaining the matrix $\mathbf{C}$, the respective centroids of coordinates of the closed curves are estimated, which

indicate the locations of brightness centers. Multiple brightness centers can be identified in this way but some steps are needed to avoid redundant locations. The steps are as follows:

[13] 1. For convenience, the brightness values are scaled from 0 to 100 in using the contour function. The number of contour levels, n, is arbitrary but nine are employed here. As a result of $n = 9$, the brightness centers with the brightness smaller than one-tenth of the strongest brightness are discarded.

[14] 2. The sequences of the curves contained in the matrix $\mathbf{C}$ are sorted in descending order according to the height of contour level.

[15] 3. The first closed curve in the matrix $\mathbf{C}$, which corresponds to the highest contour level, is examined first to obtain a centroid of the coordinates. Any following closed curves enclosing the first estimated centroid are considered to have the same centroid and so are ignored. Only the closed curves without any estimated centroids inside them are processed.

[16] 4. The closed curves encompassing the valleys of brightness distribution should be excluded. This can be done by two steps: (a) ignore the closed curves with the lowest contour level, (b) select five to seven points (in x or y direction) around the estimated centroid and use a quadratic equation, $Ax^2 + Bx + C$, to fit the data. The coefficient A should be negative if the centroid is around the peak. On the contrary, $A > 0$ indicates the location of a valley and so the resultant centroid is ignored.

[17] The above procedure is employed for two-dimensional brightness distribution. In case of a one-dimensional brightness distribution, such as the ROW and COL modes, we can extend the brightness value to two dimensions by setting a Gaussian curve in the added dimension for each brightness value, with the brightness value being the peak magnitude of the auxiliary Gaussian curve. The standard deviation of the auxiliary Gaussian curve is arbitrary since it does not bias the locations of brightness centers in the one-dimensional brightness distribution.

[18] We show two examples in Figure 2 to demonstrate the above locating approach. Figure 2a presents two original brightness distributions observed. In the SA mode (left panel), a duplicate two-blob pattern is seen, which reveals the grating pattern arising from finite spatial distances between receiving antenna groups. The folding/aliasing angles are ∼16° and ∼21°, respectively, in zonal and meridional directions. In the ROW mode (right panel), however, only the zonal distribution can be resolved because the receiving antenna groups are aligned in zonal direction. It can be found that the folding/aliasing angle is ∼42°. On the other hand, the COL mode observes only the brightness distribution in meridional direction (not shown here). It deserves to

(a)

(b)
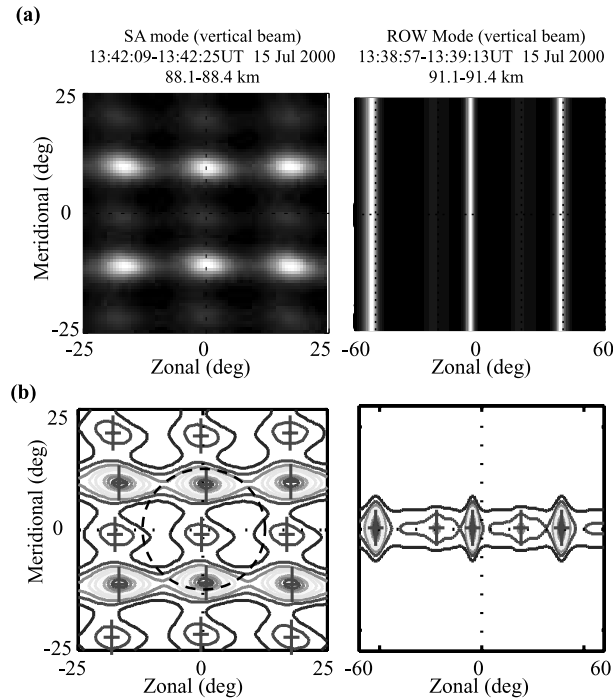
Figure 2. (a) Brightness distribution estimated with Capon's method. (left) SA mode. (right) ROW mode. (b) Contour plots of the brightness distributions shown in Figure 2a. The plus indicates the angular location of the brightness center estimated. The dashed circle encloses the region of 12.5° zenith.

mention that these observed folding/aliasing angles are consistent with our simulation calculations of CRI (not shown here), which were carried out by modeling a Gaussian-distributed echoing structure at the zenith. Moreover, simulation calculations demonstrate that it is possible to resolve two highly localized echoing centers separated by the distance larger than 2° zenith, indicating the angular resolution is close to 2°.

[19] Figure 2b shows the locating results. As expected, the brightness centers are determined explicitly and the "valleys" are excluded, even if there are fifteen brightness centers in the image of SA mode. Note that the locating approach estimates all brightness centers but does not determine which ones are the true or aliasing. For example, in the left panel of Figure 2b three brightness centers are found within the region of ±12.5° zenith (indicated by the dashed circle) but one of the two centers close to the edge of the dashed circle is aliasing.

[20] It should be mentioned that in theory the weighting effect of radar beam pattern on the brightness

distribution should be removed. However, irrational brightness peaks will appear frequently at large zenith angles after correction, suggesting the correction of data with the theoretical beam pattern is still problematic. The possible error of the estimated echo centers is thus discussed in more detail in section 4.
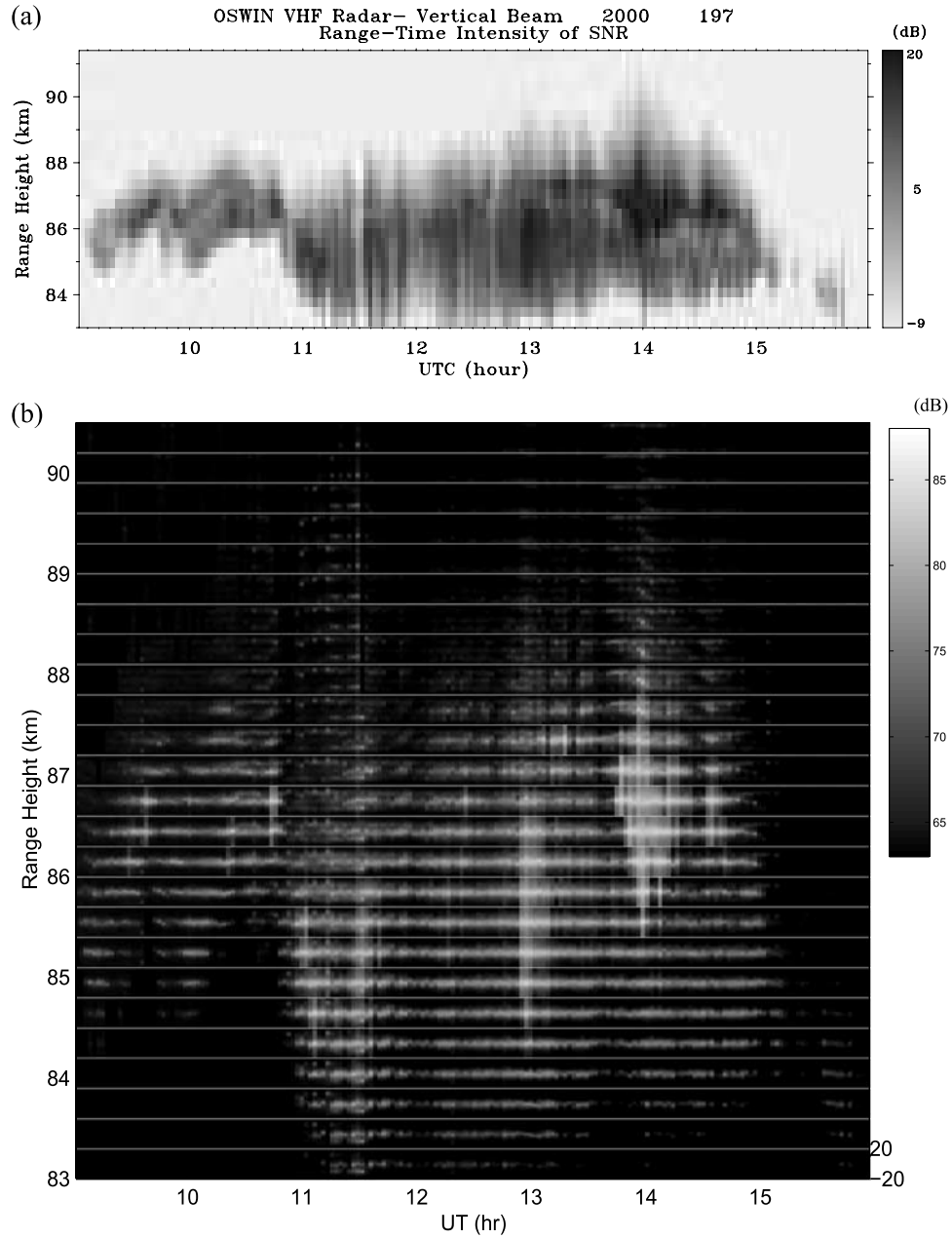
3. Observation of Multiple Echo Centers

[21] Figure 3a displays the height-time intensity of signal-to-noise ratio (SNR) of a MSE layer observed by the vertical radar beam using the whole antenna array. *Chen et al.* [2004] have used the data of SA mode for the study of aspect sensitivity. In this study, we examined the data of ROW and COL modes collected in the same period.

[22] Figure 3b presents the time variation of brightness for consecutive range gates observed by vertical COL mode. In the lower portion of the layer (below ∼86 km), the brightness distribution generally centered on the zenith (Note that there was some interference from meteors between 1100 UT and 1130 UT, these data were ignored in the CRI study). In contrast, we can observe roughly two or three patches in the brightness distribution above ∼86 km (for example, at ∼88 km between 1300 UT and 1500 UT), which appear frequently during the whole period of the observation. Such feature can also be seen in the brightness distribution of ROW mode (not shown).

[23] To view the range variation of brightness distribution more clearly, Figure 4 demonstrates some examples resolved by the vertical ROW and COL modes around the time of 1400UT. Indeed, two or three brightness patches can be identified in the upper range gates: one is around the zenith (the radar beam direction) and others are on both sides of the zenith. The brightness patches on both sides of the zenith exhibit three noticable features: (1) their zenith locations increase with ascendant altitude and get closer to 20° zenith at upper height, (2) they may appear symmetrically or arise mainly on one side, e.g., after and before 14.02 hr in the COL mode, respectively, and (3) their brightness values can be larger than those around the zenith. These features have drawn our attention to examine the multiple brightness centers more extensively, in which the angular locations of multiple brightness centers were estimated with the locating approach described in section 2.

[24] Figures 5a and 5b show the distribution of the angular locations during 09:00−15:00 UT for the vertical COL and ROW modes, in which only the data with SNR ≥ 0.25 were adopted. Note that the distribution is exhibited between −60° and 60° zenith for a more complete inspection. According to the repeated groups of angles, we conclude that the groups of angles between −20° and 20° zenith are not ambiguous. With this in

(a)

(b)

Figure 3. (a) Height-time intensity plot of signal-to-noise ratio (SNR) of the MSE layer observed by the vertical radar beam using the whole antenna array. (b) Time variation of brightness at consecutive range gates, observed by vertical COL mode. 1024 data points were used for each imaging, corresponding to ~16-s time resolution. Scanning angle range is −20° to 20° zenith.

mind, we can focus on the angular region between −20° and 20° zenith (indicated by two vertical dashed lines) and find three groups of angles above the range height of ~86 km. The central group of angles should be related to the echoes scattered/reflected from the main radar beam while the two side groups of angles are worthy of study further. Moreover, in the ROW mode the two side groups of angles are not as symmetric as in the COL mode,
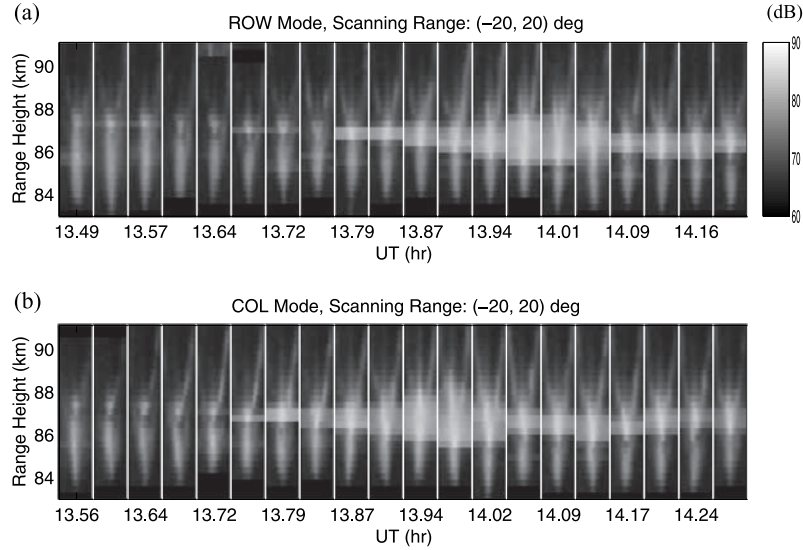
Figure 4. Range variation of brightness distribution, observed by (a) vertical ROW mode and (b) vertical COL mode, respectively. 1024 data points were used for each imaging, corresponding to ~16-s time resolution. Scanning angle range is $-20°$ to $20°$ zenith.

namely, the left group of angles disappears eventually above the range height of ~89 km. This feature is also worth clarifying.

[25] In addition to vertical mode, the data collected by the 7°-oblique COL and ROW modes were also examined. Figure 5c exhibits one example observed by the oblique ROW mode (7° zenith in the eastern direction). Notice that only the groups of angles between $-20°$ and $20°$ are reliable; others are aliasing. In the lower gates (<86 km) the groups of angles around the direction of radar beam are mostly smaller than 7° and increase as range height increases. The angle smaller than 7° is in agreement with a low effective angle due to enhanced aspect sensitivity [*Hocking et al.*, 1986]. Such feature indicates that this MSE layer possesses stronger aspect sensitivity in the lower part and becomes more turbulent along the height, which has been demonstrated by *Chen et al.* [2004]. The brightness centers above the range height of ~86 km are more complex, we depict them as follows: the group of angles around the direction of main radar beam eventually splits into two parts- one is around 7° zenith and the other is close to 20° zenith. The group of angles around 7° zenith should be the echoes returning from the main radar beam; however, the group of angles close to 20° zenith as well as that close to -20° zenith may arise from the same causes as those in the vertical COL and ROW modes. Such features were also observed by other oblique-ROW and COL modes (not shown). Based on Figures 3−5, we discuss the possible causes
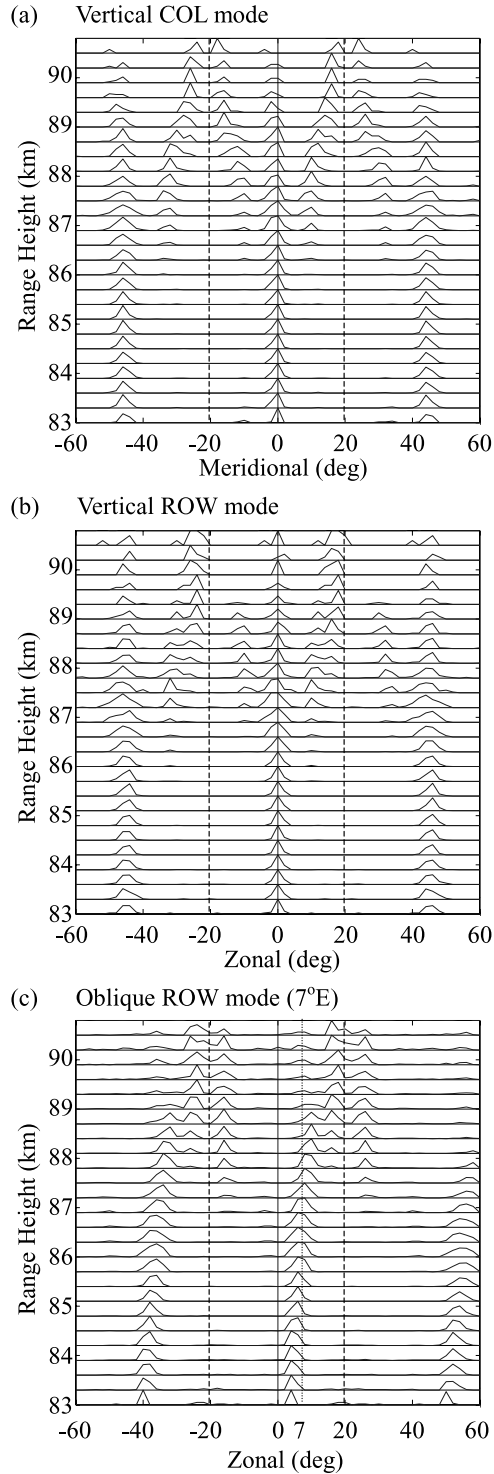
responsible for the echo centers beyond the viewing region of the main radar beam in the following section.

4. Discussion

4.1. Effect of Radar Beam Pattern

[26] As mentioned, in theory the weighting effect of radar beam pattern on the brightness distribution should be removed to obtain a more accurate estimate of echo center. This thought, however, might not be achieved effortlessly because irrational brightness peaks will appear at large zenith angles after correction. Instead, we examined the possible error of estimated angles according to the radar beam patterns shown in Figures 1b and 1c.

[27] Modeling the scattering/reflecting echo distribution by a Gaussian function, $\exp[-(\theta-\theta_o)^2/2\theta_s^2]$, where θ_o is the echo center and θ_s is the standard deviation, and then estimating the product of this Gaussian function and radar beam pattern, the product can demonstrate the brightness distribution theoretically. Here the radar beam pattern should be the product of transmitting and receiving beam patterns and so we employed the beam patterns shown in Figure 1b. Some results are shown in Figure 6, where $\theta_s = 1°$, $2°$, and $3°$, respectively, in Figures 6a, 6b, and 6c. Clearly, for narrow-distributed echoes in Figure 6a the resultant brightness distribution is less deformed and its maximum is also less biased. On the other hand, multiple brightness maximums may come up
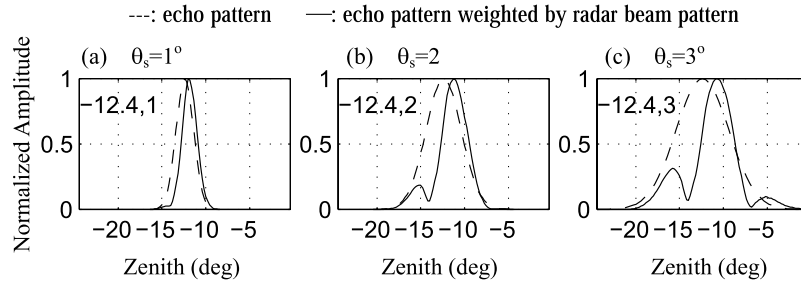
Figure 5. Distribution of angular locations of brightness centers in (a) meridional direction observed by vertical COL mode, (b) zonal direction observed by vertical ROW mode, and (c) zonal direction observed by the 7°E-oblique ROW mode, in which the distribution at each gate is self-normalized. 128 data points were used for each CRI analysis, corresponding to ~2-s time resolution for each calculation of brightness center. Data time interval: 0900–1500 UT. Adoption threshold: SNR ≥ 0.25.

for wide distributed echoes in Figures 6b and 6c. To determine the angular locations of these multiple brightness maxima, we employ again the locating approach introduced in the section 2. A thorough estimation is shown in Figure 7.

[28] The abscissa of Figure 7a is the zenith angle of echo center given in the model, and the ordinate on left indicates the angle difference between estimated and given echo centers (estimated minus given). For example, for 1°-distributed echo pattern the echo center given at 8° zenith results in two values of $\Delta\theta$ at ~0.5° and ~−2° (see the thick-black curves), hence leading to two centers estimated around $8° + 0.5° = 8.5°$ and $8° − 2° = 6°$ zenith. Similarly, two centers around $8° + 1° = 9°$ and $8° − 2.5° = 5.5°$ zenith are estimated for the 2°-distributed echo pattern. Even three centers could be produced in the 3°-distributed echoes, e.g., at the given zenith angle of 11° the estimated centers are about $11° + 4.5° = 15.5°$, $11° − 1° = 10°$ and $11° − 6.5° = 4.5°$, respectively. Some of these centers, however, may not be detectable due to their extremely low intensity (can be as low as −25 dB, as indicated by the thick-gray curves). On the other hand, the zenith angles given within the beam width produce only single center although the single center estimated is still biased except at the zenith. It is obvious that broader distributed echo pattern causes larger angular bias of the estimated center. Unbiased center occurs only when the center of echo pattern is around the maximums of main lobe and side lobes of the beam pattern. It should be mentioned that such angular bias should have upper limitation, as the Gaussian echo pattern gets broader and broader. Considering the extreme case of a uniform echo pattern, the estimated echo centers will occur at the maximums of main lobe and sidelobes. Except for the echo center at the main lobe, however, other echo centers can be thought to be the biased ones if they are detectable.

[29] Figure 7b presents another relationship between estimated and given echo centers. The abscissa is now the estimated zenith angle of echo center and the ordinate on left indicates the angle difference between estimated and given echo centers (estimated minus given). For example, for 1°-, 2°- and 3°-distributed echo patterns the values of $\Delta\theta$ for the zenith angle estimated at 4° are

Figure 6. Echo distribution (solid curve) resulting from the simulation using a Gaussian-distributed echoing structure (dashed curve) weighted by the beam pattern shown in Figure 1b. The two numbers on the top left corner of each panel are the center and standard deviation (in degree) of the echoing structure given in the simulation.
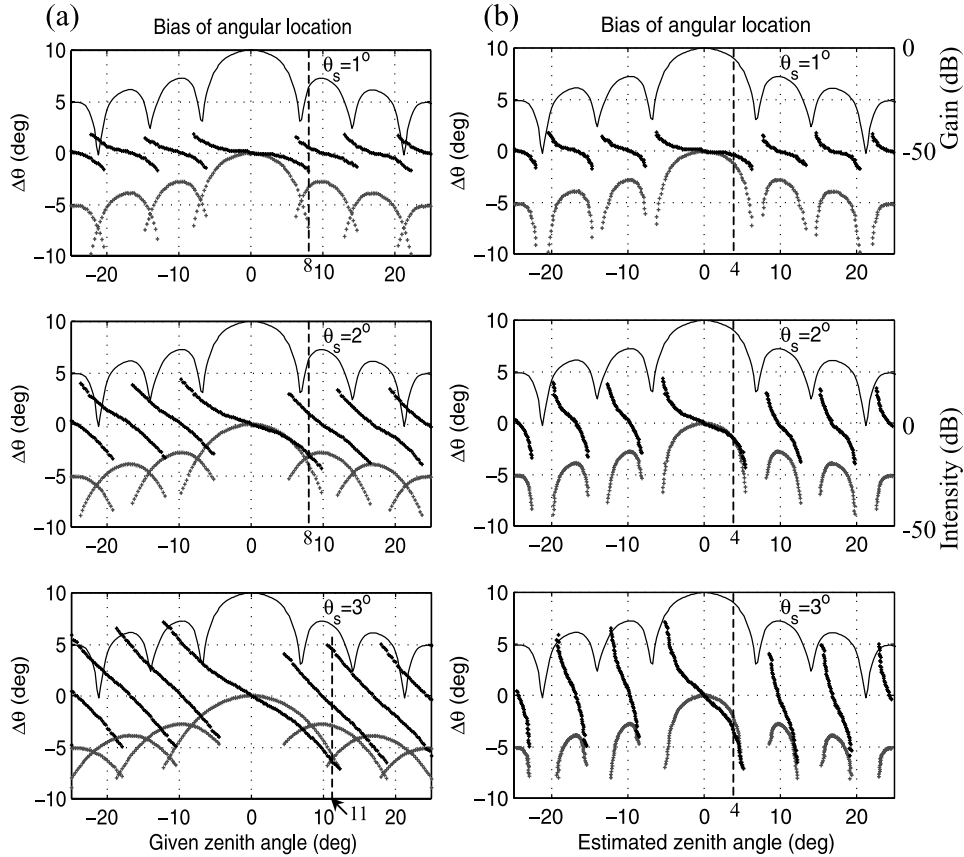
Figure 7. Angular Bias of echo center ($\Delta\theta$). Left ordinates indicate angle difference (thick-black curve) between estimated and given echo centers (estimated minus given). (a and b) The abscissas are, respectively, the given and estimated zenith angles of echo centers. Thin solid curve shows the two-way beam pattern, with the scale of -50 dB to 0 dB shown at right ordinate of the topmost panel in Figure 7b. Thick-gray curve is the intensity of estimated echo center, with the scales of -50 dB to 0 dB shown at right ordinate of the middle panel in Figure 7b.

about $-0.5°$, $-1.5°$, and $-3.5°$, respectively, which means that the estimated echoes originate from the given echo patterns centering on $4° + 0.5° = 4.5°$, $4° + 1.5° = 5.5°$, and $4° + 3.5° = 7.5°$, respectively. As mentioned, however, not all the echo centers are detectable because of their low intensity. Let the detectable intensity be larger than -20 dB, we will only have the zenith angles estimated within the main lobe as well as the first and second sidelobes. This argument can verify the reality of the brightness centers observed within $20°$ zenith in Figure 5 and suggests the maximum biases of estimated brightness centers are about $±5°$. Certainly, the angular bias of echo center is also related to the echo pattern; here the Gaussian distribution with several degrees of standard deviation is an acceptable model.

[30] Figure 7b also indicates that we will miss the echo centers around the notches of the beam pattern. According to the beam patterns shown in Figure 1, the notches within $±20°$ zenith locate at $\sim±7°$ and $\sim±14°$ zenith for vertical beam pattern, and $0°$, $\sim-7°$, and $\sim±14°$ zenith for 7°E-oblique beam pattern. In Figure 5a, the lack of echo center at $\sim±7°$ zenith is evident but cannot be seen at $\sim±14°$ zenith. In comparison, Figure 5b indeed shows a lack of echo center at $\sim14°$ zenith between ~88 km and ~89 km and Figure 5c also demonstrates this. After inspecting other diagrams of angle distribution (not shown) obtained by COL and ROW modes, we can find roughly the lack of echo center at other expected angular places.

[31] The above investigation demonstrates the effect of radar beam pattern on echo center. In theory, we may need to consider the receiving pattern of Capon CRI, which is adaptive to the echo pattern but with a maximum gain in the direction where the brightness is to be estimated [Palmer et al., 1998]. However, as shown in Figure 7, the echo centers coming from the first and second sidelobes already have quite low intensity (<-12 dB). Additional weighting of the adaptive receiving pattern will cause even lower intensity outside the scanned direction, contributing tiny part to the brightness value. In view of this, we ignore the adaptive receiving pattern of Capon CRI in our present examination. Moreover, the radar beam patterns obtained with simulation software are idea ones. Real radar beam patterns may need other methods to prove, such as using the radio star, the beacon signal from the satellite, or the experiment with an airplane passing through the radar array. With these limitations and neglect, Figure 7 provides rough estimate of bias of the observed echo center.

[32] To summarize, the observed echo centers may be biased by several degrees according to Figure 7, but it does not mask the fact that some echoes indeed returned from large off-zenith angles. Possible mechanisms responsible for the echoes at large off-zenith angles are discussed below.

4.2. Mechanisms of the Echoes at Large Off-Zenith Angles

[33] The echoes observed at large off-zenith angles are not within the same height interval as those in the main radar beam. For example, for the objects at the range of 90 km with the zenith angles of $10°$ and $17°$, their true heights are ~88.6 km and ~86 km, respectively. There is about $1.4-4$ km difference between the range and the height of the object, corresponding to about $5-14$ range gates in the 300-m sampling step. In view of this, for a vertical radar beam the atmospheric echoes returning from large off-zenith angles should originate from the places below the height of the sampling gate. These echoes may enter from the first and second sidelobes of the radar beam pattern. For example, around 1400 UT the echo intensity was observed to be about 87 dB at the height of 86 km (Figure 3b). If the echo comes from the direction of $17°$ zenith, it will appear at the sampling range of ~90 km. The echo intensity is about 67 dB due to the 20-dB attenuation of the radar beam pattern (Figure 1b), which is indeed detectable at times, as Figure 4 shows. Same inspection can also be made for the 7°-oblique radar beam but now the echoes may enter from the first to third sidelobes on the left side of main lobe and the first sidelobe on the right side of main lobe (Figure 1c).

[34] The above discussion suggests that the echo centers at lower heights can be observed at large off-zenith angles at higher range gates in the ROW and COL modes experiments, although it may only occur at some occasions. To go further, we would like to examine another geophysical mechanism producing the echoes at large off-zenith angles for present and future studies.

[35] In the literature, Röttger et al. [1990] pointed out that more than one reflection point at a time can occur in a partially reflecting surface undulated by a bump. Besides, Meek and Manson [1992] used their "glint theory" to simulate the variations of reflection points for a sinusoidally perturbed, horizontally stratified, partially reflecting layer, and showed multiple reflection points in a range gate; moreover, the incident angles of the reflection points are more off zenith when the amplitude of the sinusoidally modulated layer is larger. Using similar simulation method, Yu et al. [2001] also verified the above features of multiple reflection points and showed that multiple reflection points may occur in consecutive range gates by giving many randomly distributed sinusoidal layers with synchronized phase and same amplitude. However, a more physical feature of the wave-modulated reflecting layers is that the waves near the breaking height may increase in amplitude and then the wave shape steepens during the saturation process [e.g., Mobbs, 1985; Weinstock, 1986]. Recently, the influence of waves on layered PMSE structures was
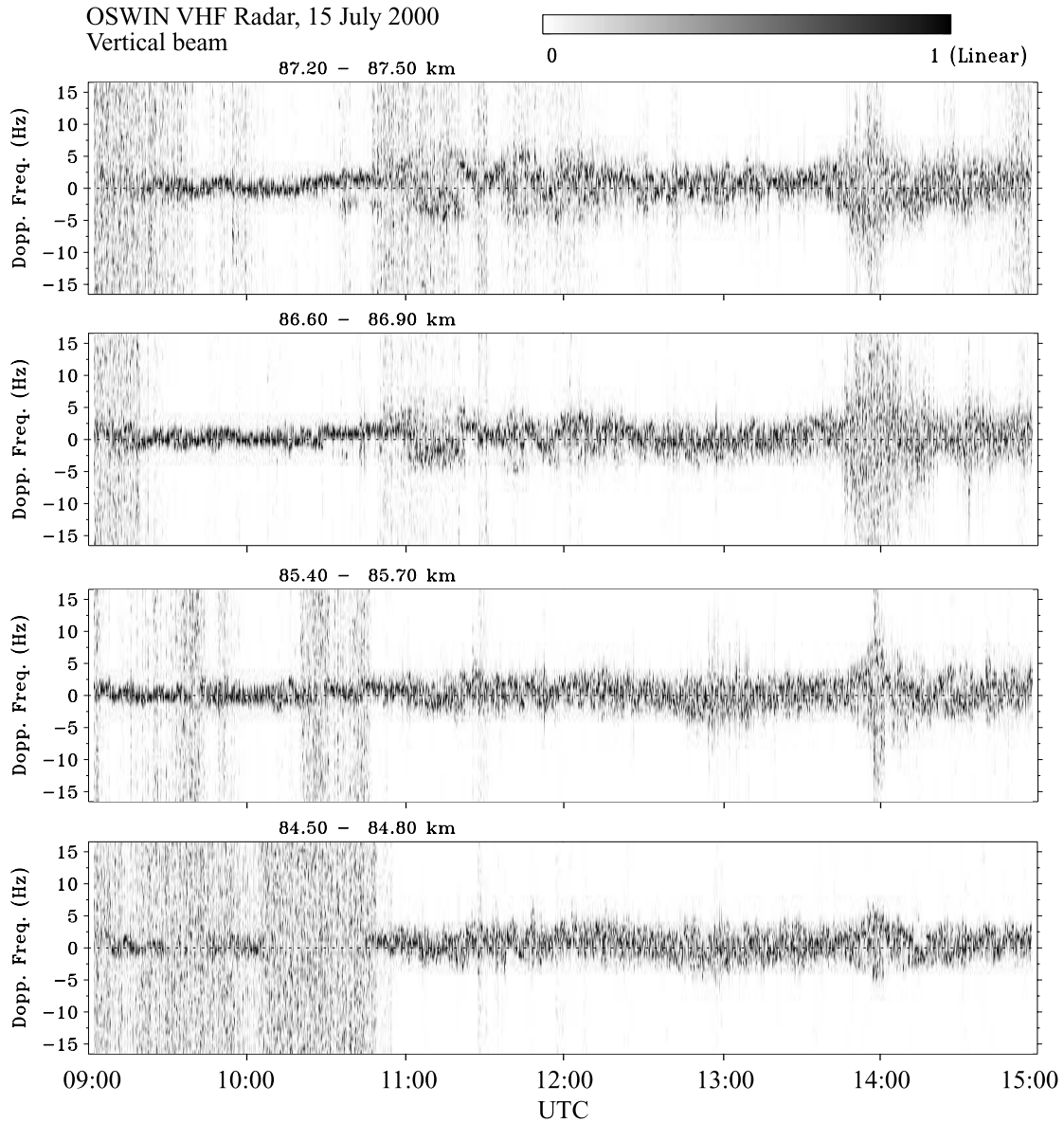
Figure 8. Spectrograms at four sampling gates for the vertical radar beam using the whole antenna array. Spectral intensity is self-normalized and exhibited in linear scale.

simulated successfully with a microphysical model [*Hoffmann et al.*, 2005], which demonstrated that gravity waves play an important role on the layering processes. Referring to these studies, we wonder whether wave activities exist in our present MSE layer or not. A simple investigation is shown in Figures 8 and 9.

[36] Figure 8 displays four spectrograms at different heights observed by the vertical beam using the whole antenna array. It is clear that the oscillation in the

spectrogram grows with height between ~11:00−12:30 UT and after ~13:30 UT. Similar spectral feature was reported before [*Miller et al.*, 1993; *Yu et al.*, 2001]. *Miller et al.* [1993] suggested that upward-propagating and steepened gravity waves could be a cause of this spectral feature. The wave activities can be further indicated by vertical wind, as shown in Figure 9. Figure 9a highlights the feature of upward and downward winds at different times and altitudes, revealing that

(a)

OSWIN-Radar Vertical Wind Field   2000 197

(b)
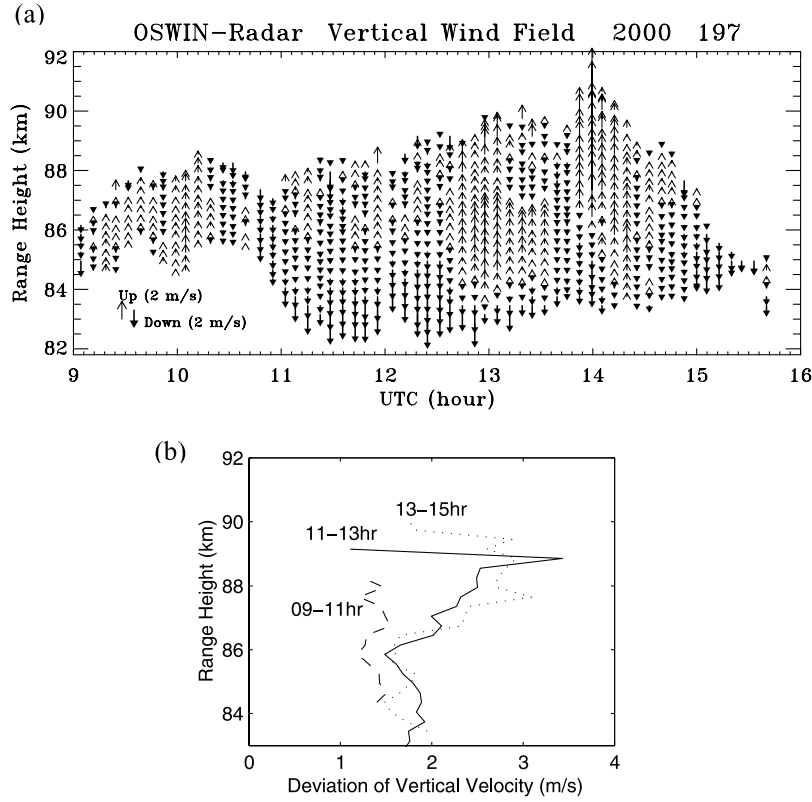
Figure 9.   (a) Vertical wind field, showing the upward and downward motions. (b) Mean profiles of standard deviations of vertical velocities in three different time intervals.

the vertical velocities changed their directions in various periods from tens of minutes to over one hour. Figure 9b shows the standard deviations of vertical velocities in three different time intervals. Except for the first time interval (from 0900−1100 UT), the standard deviations of vertical velocities above ∼86 km became larger as the altitude increased. Notice that the abrupt decrease of the standard deviations at the height close to 90 km is due to much fewer data points available. Overall, Figures 8 and 9 indicate the waves were more and more active above ∼86 km.

[37]   Since wave activities existed in the MSE layer, we extended the works made by *Meek and Manson* [1992] and *Yu et al.* [2001] and carried out some simulations. The scenario is as follows:

[38]   1. The wave-modulated structure is represented in the form

$$z(t) = H_o + A_z cos(kx + \omega t + \phi_h), \qquad (2)$$

where H_o and A_z are, respectively, the average height and amplitude of the wavy structure, k is the horizontal wavenumber, ω is the intrinsic wave frequency, and ϕ_h is the phase of the wave at different heights. By adding ϕ_h,

we have considered the vertical propagation of the wave, or, the vertical wavelength.

[39]   2. Horizontal and vertical wavelengths are 20 km and 6 km, respectively. Intrinsic wave period is 10 min. A_z is 50 m below 86 km; above 86 km, however, A_z increases 50 m per hundred meters in height. The boundary height of 86 km is selected in view of more active waves observed above this height.

[40]   3. Nine hundreds reflecting surfaces, modulated by the form of (2), are given between 83 km and 92 km and so the distance between adjacent surfaces is 10 m. The distance between adjacent surfaces can be larger so that the number of reflecting surfaces can be fewer to save time in computation. For example, ninety reflecting surfaces with 100-m distance between two surfaces are also workable. However, if the number of layers is too small, say, ten layers, the reflection points received may be few and cause the distribution fragmented.

[41]   4. The reflection point is defined as the location where the ray path is perpendicular to the surface of the modulated structure. Based on this, the criterion, −1.01 < (the slope of the ray path) × (the slope of the surface) < −0.99, is used here to adopt the reflection point. The
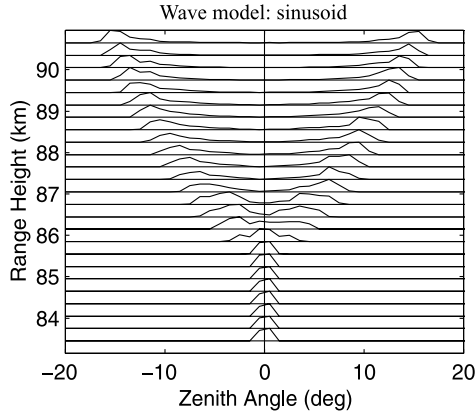
Figure 10. Distribution of reflection points resulting from the model of sinusoid-modulated and growing-amplitude layer structure, in which the distribution at each gate is self-normalized. The amplitude of the wave below 86 km is 50 m, but grows 50 m per 100 m in height above 86 km.

travelling time, t is 10 min (one period of the wave) and all reflection points in the horizontal range between −50 km and 50 km, corresponding to the zenith angle interval between −35.5° and 35.5° at the height of 86 km, are estimated. The reflection points are classified according to their ranges, not height. As a result, the reflection points in the same range gate may return from different zenith angles. Notice that the reflection points are not limited within the 6°-transmitted beam width.

[42] A consequent distribution of reflection points is shown in Figure 10. One can see a symmetric pattern of reflection points above ∼86 km, with increased zenith angles along the altitude. Such a distribution of reflection points is analogue to that observed in Figure 5a. Various wavelengths and amplitudes of the waves may result in the features similar to Figure 10. The set of wave parameters employed here is just one case to demonstrate the observed features. Moreover, the scattering echoes from vertical direction are not considered in the simulation model and so only few reflection points come from the zenith, causing the lack of central group of angles above ∼86 km.

[43] We can also simulate the reflecting surfaces tilted asymmetrically by wave breaking or wind shear. To examine this, the wave shape, $z = x^b(1-x)^c$, is assumed (Figures 11a and 11b), and the wavelengths and amplitudes of the waves in the preceding simulation are employed again. The wave shape used here is not unique; any formulated waveform that can illustrate asymmetrically tilted wave shapes is workable. The resultant distribution of reflection points is shown in

Figure 11c, in which we observe an asymmetric pattern of reflection points above ∼86 km. This feature seems to resemble that seen in Figure 5b.

[44] To understand more the above simulation, a schematic plot of growing amplitude, asymmetrically tilted layers is depicted in Figure 12. Please see the reception at the time t_2. Owing to the asymmetric tilted layers, the reflecting echoes coming from the left side (arrow-
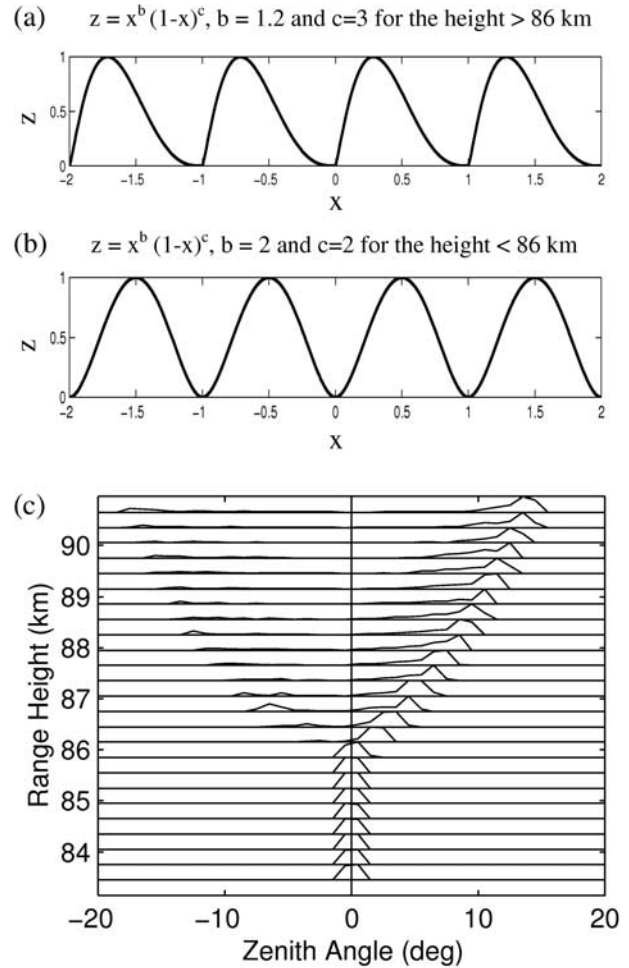
Figure 11. (c) Distribution of reflection points resulting from the model of wave-modulated and growing-amplitude layer structure, in which the distribution at each gate is self-normalized. Differing from the sinusoidal wave model in Figure 10, the waveform of $z = x^b(1 - x)^c$ is employed. (a and b) The wave shapes are used at the heights above and below 86 km, respectively. The amplitude of the wave below 86 km is 50 m, but grows 50 m per 100 m in height above 86 km.
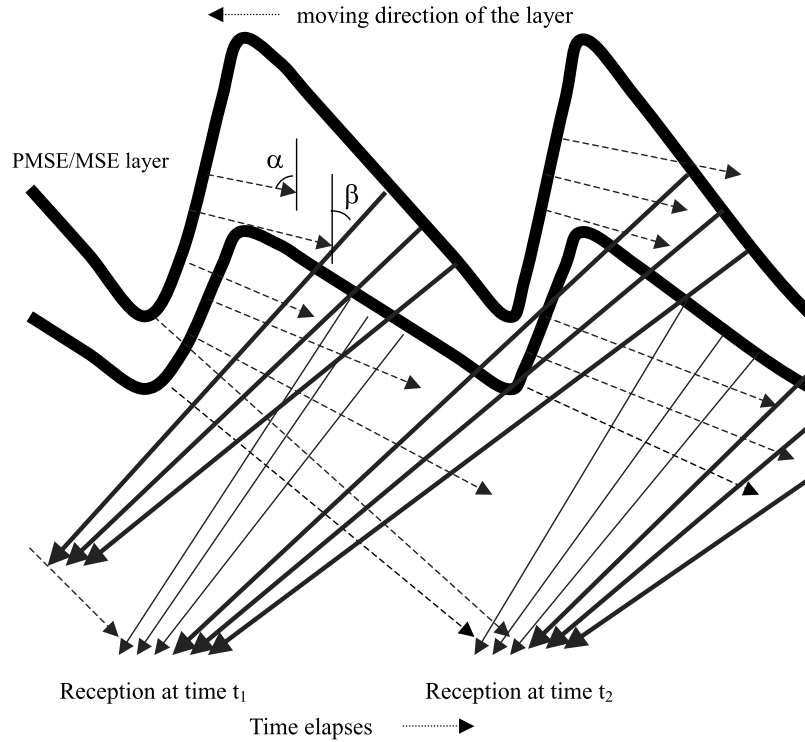
Figure 12. Schematic diagram of reflection points due to the wave-modulated, growing-amplitude, and asymmetrically tilted layer structures. α and β denote the zenithal incident angles, $\alpha > \beta$.

headed dash lines) usually have larger incident angles (indicated by α) than those (indicated by β) coming from the right side (arrow-headed solid lines). Therefore, it is more difficult to receive the reflecting echoes from the left side. As a result, the reflecting echoes coming from the right side dominate the distribution of incident angles. Moreover, the reflecting echoes originating from the upper layer have larger incident angles (thicker arrow-headed solid lines), which will emerge in the higher sampling gates because of their longer ranges. This explains the simulated result shown in Figure 11c.

[45] Finally, three points should be emphasized: (1) the phase shift (ϕ_h), horizontal progress (t), and increasing amplitude (A_z) of the structure are considered in the simulation. The increasing amplitude of the structure is essential in the simulation to produce two groups of reflection points with gradually separated angular positions on both sides of the zenith; (2) not all of these reflecting echoes can be received in actual observation because the radar beam pattern plays an important role. That is, the reflecting echoes around the notches of the beam pattern may not be detectable due to their extremely low intensity; and (3) we use the model of wavy layers to simulate the reflecting surfaces, in which

the reflecting surfaces may indeed exist or are due to anisotropic irregularities.

5. Conclusions

[46] This paper has presented some features of multiple echo centers in a thick mesosphere-summer-echo (MSE) layer with the coherent radar imaging (CRI) realized by the six-receiver OSWIN VHF radar. A contour-based approach, which is different from the fitting method with a Gaussian function, has developed to locate multiple echo centers. The locating approach is very helpful for present and future researches. We also examined the error of observed echo center by the simulation with a Gaussian-distributed echoing structure, and found that several degrees of error are possible. In spite of several degrees of error, some echoes indeed returned from large off-zenith angles (several to ~20°) in our observations.

[47] In the lower portion (below ~86 km) of the MSE layer examined, the echo centers clustered around the main lobe of the radar beam pattern and exhibited evident aspect sensitivity. In the upper portion of the layer; however, three groups of echo centers were

observed. The central group of echo centers was related to the scattering/reflecting echoes within the main lobe of the radar beam pattern but the two side groups of echo centers, which were getting off the zenith by several to ~20 degrees at higher sampling gates, were only accessible to wide receiving beam width like the COL and ROW modes employed in this study. The two side groups of echo centers were likely to be the echoes returning from the sidelobes of the radar beam pattern, which originated from the echoing structures at lower height and were received at higher sampling gate. Such feature may not be found in all observations but it deserves to take into account for the thick layer structures in the mesosphere.

[48] In addition to the above mechanism, we also demonstrate that wave-modulated, partially reflecting structures, in which the wavy reflecting structures are possessed of growing amplitudes with the altitude, can also result in getting off-zenith angles of echoes at higher sampling gates. Moreover, the wavy reflecting structures may be tilted asymmetrically to induce asymmetric numbers of reflection points on both sides of the radar beam, yielding a potential explanation of the observation.

[49] It is highly expected that wave parameters (period, wavenumber, and so on) can be retrieved from the CRI data. However, considering that the reflection points estimated from the brightness distribution have not been properly corrected with the radar beam pattern in this study, especially at large zenith angles, we reserve this part in future researches when more precise function/processing in correcting the brightness distribution can be employed. In the future, the tilted refractivity structures may be verified further with some more observational techniques such as multiple-frequency interferometry. Multiple-frequency interferometry can resolve the layers imbedded in the radar volume, providing an opportunity to survey the detailed variation in the PMSE/MSE layer structures [*Chilson et al.*, 2001; *Fernandez et al.*, 2005] and then reveal a clearer appearance of wave activities (origination, growth, and dissipation or breaking). With clearer layer structures, it is also expected that we can distinguish the mechanisms of the echo centers at large-off zenith angles, namely, originating from the scattering structures at lower height or from the wavy reflecting structures. Thus it is beneficial to incorporate the multiple-frequency technique with the multiple-receiver observation of the PMSE/MSE.

References

Bremer, J., P. Hoffmann, R. Latteck, and W. Singer (2003), Seasonal and long-term variations of PMSE from VHF radar observations at Andenes, Norway, *J. Geophys. Res.*, *108*(D8), 8438, doi:10.1029/2002JD002369.

Capon, J. (1969), High-resolution frequency-wavenumber spectrum analysis, *Proc. IEEE*, *57*, 1408–1419.

Chen, J.-S., P. Hoffmann, M. Zecha, and J. Röttger (2004), On the relationship between aspect sensitivity, wave activity, and multiple scattering centers of mesosphere summer echoes: A case study using coherent radar imaging, *Ann. Geophys.*, *22*, 807–817.

Chilson, P. B., P. Czechowsky, J. Klostermeyer, R. Rüster, and G. Schmidt (2001), Frequency domain interferometry mode observations of PMSE using the EISCAT VHF radar, *Ann. Geophys.*, *18*, 1599–1612.

Chilson, P. B., T.-Y. Yu, R. D. Palmer, and S. Kirkwood (2002), Aspect sensitivity measurements of polar mesosphere summer echoes using coherent radar imaging, *Ann. Geophys.*, *20*, 213–223.

Cho, J. Y. N., and M. C. Kelley (1993), Polar mesosphere summer echoes: Observations and current theories, *Rev. Geophys.*, *31*, 243–256.

Cho, J. Y. N., and J. Röttger (1997), An updated review of polar mesosphere summer echoes: Observations, theory and their relationship to noctilucent clouds and subvisible aerosols, *J. Geophys. Res.*, *102*, 2001–2020.

Czechowsky, P., and R. Rüster (1997), VHF radar observations of turbulent structures in the polar mesopause region, *Ann. Geophys.*, *15*, 1028–1036.

Czechowsky, P., R. Rüster, and G. Schmidt (1979), Variations of mesospheric structures in different seasons, *Geophys. Res. Lett.*, *6*, 459–462.

Ecklund, W. L., and B. B. Balsley (1981), Long-term observations of the Arctic mesosphere with the MST radar at Poker Flat, Alaska, *J. Geophys. Res.*, *86*, 7775–7780.

Fernandez, J. R., R. D. Palmer, P. B. Chilson, I. Häggström, and M. T. Rietveld (2005), Range imaging observations of PMSE using the EISCAT VHF radar: Phase calibration and first results, *Ann. Geophys.*, *23*, 207–220.

Hélal, D., M. Crochet, H. Luce, and E. Spano (2001), Radar imaging and high-resolution array processing applied to a classical VHF-ST profiler, *J. Atmos. Sol. Terr. Phys.*, *63*, 263–274.

Hocking, W. K., R. Rüster, and P. Czechowsky (1986), Absolute reflectivities and aspect sensitivities of VHF radio wave scatterers measured with the SOUSY radar, *J. Atmos. Terr. Phys.*, *48*, 131–134.

Hoffmann, P., W. Singer, and J. Bremer (1999), Mean seasonal and diurnal variations of PMSE and winds from 4 years of radar observations at ALOMAR, *Geophys. Res. Lett.*, *26*, 1525–1528.

Hoffmann, P., M. Rapp, A. Serafimovich, and R. Latteck (2005), On the occurrence and formation of multiple layers

of polar mesosphere summer echoes, *Geophys. Res. Lett.*, *32*, L05812, doi:10.1029/2004GL021409.

Huaman, M. M., and B. B. Balsley (1998), Long-term-mean aspect sensitivity of PMSE determined from Poker Flat MST radar data, *Geophys. Res. Lett.*, *25*, 947–950.

Huang, C.-M., E. Kudeki, S. J. Franke, C.-H. Liu, and J. Röttger (1995), Brightness distribution of midlatitude E region echoes detected at Chung-Li VHF radar, *J. Geophys. Res.*, *100*, 14,703.

Hysell, D. L. (1996), Radar imaging of equatorial F region irregularities with maximum entropy interferometry, *Radio Sci.*, *31*, 1567–1578.

Hysell, D. L., and R. F. Woodman (1997), Imaging coherent backscatter radar observations of topside equatorial spread F, *Radio Sci.*, *32*, 2309–2320.

Kudeki, E., and F. Sürücü (1991), Radar interferometric imaging of field-aligned plasma irregularities in the equatorial electrojet, *Geophys. Res. Lett.*, *18*, 41–44.

Latteck, R., W. Singer, and J. Höffner (1999), Mesosphere summer echoes as observed by VHF radar at Kühlungsborn (54°N), *Geophys. Res. Lett.*, *26*, 1533–1536.

Meek, C. E., and A. H. Manson (1992), Angle-of-arrival oscillation in the mesosphere as seen by medium frequency (MF) radar, *J. Atmos. Terr. Phys.*, *54*, 277–293.

Miller, C. A., W. E. Swartz, and J. Y. N. Cho (1993), CUPRI observations of PMSE during SALVOC of NLC-91: Evidence of a depressed mesopause temperature, *Geophys. Res. Lett.*, *20*, 2295–2298.

Mobbs, S. D. (1985), Propagation of nonlinear internal gravity waves at stratospheric and mesospheric heights. Part III: The wave shape, *Ann. Geophys.*, *3*, 599–608.

Morris, R. J., D. J. Murphy, I. M. Reid, D. A. Holdsworth, and R. A. Vincent (2004), First polar mesosphere summer echoes observed at Davis, Antarctica (68.6°S), *Geophys. Res. Lett.*, *31*, L16111, doi:10.1029/2004GL020352.

Morris, R. J., D. J. Murphy, R. A. Vincent, D. A. Holdsworth, A. R. Klekociuk, and I. M. Reid (2006), Characteristics of the wind, temperature and PMSE field above Davis, Antarctica, *J. Atmos. Sol. Terr. Phys.*, *68*, 418–435.

Palmer, R. D., S. Gopalam, T.-Y. Yu, and S. Fukao (1998), Coherent radar imaging using Capon's method, *Radio Sci.*, *33*, 1585–1598.

Rapp, M., and F.-J. Lübken (2004), Polar mesosphere summer echoes (PMSE): Review of observations and current understanding, *Atmos. Chem. Phys.*, *4*, 2601–2633.

Reid, I. M., P. Czechowsky, R. Rüster, and G. Schmidt (1989), First VHF radar measurements of mesopause summer echoes at midlatitudes, *Geophys. Res. Lett.*, *16*, 135–138.

Röttger, J., C. La Hoz, M. C. Kelly, U. P. Hoppe, and C. Hall (1988), The structure and dynamics of polar mesosphere summer echoes observed with the EISCAT 224-MHz radar, *Geophys. Res. Lett.*, *15*, 1353–1356.

Röttger, J., C. La Hoz, S. J. Franke, and C.-H. Liu (1990), Steepening of reflectivity structures detected in high-resolution Doppler spectra of polar mesosphere summer echoes (PMSE) observed with the EISCAT 224-MHz radar, *J. Atmos. Terr. Phys.*, *52*, 939–954.

Weinstock, J. (1986), Finite amplitude gravity waves, Harmonics, advective steepening and saturation, *J. Atmos. Sci.*, *43*, 688–704.

Woodman, R. F. (1997), Coherent radar imaging: Signal processing and statistical properties, *Radio Sci.*, *32*, 2372–2391.

Woodman, R. F., B. B. Balsley, F. Aquino, L. Flores, E. Vazquez, M. Sarango, M. M. Huaman, and H. Soldi (1999), First observations of polar mesosphere summer echoes in Antarctica, *J. Geophys. Res.*, *104*, 22,577–22,590.

Yu, T.-Y., R. D. Palmer, and D. L. Hysell (2000), A simulation study of coherent radar imaging, *Radio Sci.*, *35*, 1129–1141.

Yu, T.-Y., R. D. Palmer, and P. B. Chilson (2001), An investigation of scattering mechanisms and dynamics in PMSE using coherent radar imaging, *J. Atmos. Sol. Terr. Phys.*, *63*, 1797–1810.

Zecha, M., J. Bremer, R. Latteck, W. Singer, and P. Hoffmann (2003), Properties of midlatitude mesosphere summer echoes after three seasons of VHF radar observations at 54°N, *J. Geophys. Res.*, *108*(D8), 9439, doi:10.1029/2002JD002442.

———————

J.-S. Chen, Department of Computer and Communication Engineering, Chienkuo Technology University, No. 1, Jieshou N. Rd., Changhua City 500, Taiwan. (jschen@ctu.edu.tw)

P. Hoffmann and M. Zecha, Leibniz-Institut für Atmosphärenphysik, Kühlungsborn, Germany.

C.-H. Hsieh, Department of Computer Science and Information Engineering, Chaoyang University of Technology, 41394 Taiwan.